

A NEW METHOD FOR ROTOR WAKE ANALYSIS USING NURBS PRIMITIVES

W. R. M. Van Hoydonck R. J. J. Bakker
National Aerospace Laboratory (NLR)
1059 CM Amsterdam
Netherlands

wim.van.hoydonck@nlr.nl

richard.bakker@nlr.nl

M. J. L. van Tooren
Delft University of Technology
2629 HS Delft
Netherlands

m.j.l.vantooren@tudelft.nl

Abstract

Preliminary results are presented of a new method that uses NURBS primitives to model vorticity-carrying elements of a helicopter rotor wake in a simplified form. One of the main objectives of this research is the development of a wake model that can run in real-time to aid in the area of helicopter-ship qualification testing at the NLR. The first steps towards this goal are reported in this paper. After a short introduction of the underlying geometry, a mathematical model of a NURBS-based vortex ring model is presented. This includes a derivation of the equations of motion, a validation of induced velocity calculations including core model corrections and time simulations of a single vortex ring and one of two leapfrogging rings. The paper is concluded with a presentation of preliminary results of a simplified model of the rotor wake of a helicopter in hover, including a single-step trim procedure.

Nomenclature

$B_{i,n}$	i^{th} Bernstein polynomial of degree n
C_T	rotor thrust coefficient
m	number of knots -1
N	number of rotor blades
n	number of control points -1
$N_{i,p}$	i^{th} B-spline basis function of degree p
p	degree of curve
\mathbf{P}_i	i^{th} control point
\mathbf{r}	(relative) position vector
R	vortex ring radius, helicopter rotor radius
r_c	vortex core size
$R_{i,n}$	i^{th} rational basis function of degree n
T	rotor thrust
U	knot vector
u	NURBS curve parameter
u_i	i^{th} knot
\mathbf{v}	speed vector
v_h	induced velocity in hover
V_z	vortex ring self-induced velocity
V_θ	swirl velocity
w_i	weight of i^{th} control point, weight of i^{th} quadrature point
Γ	circulation strength
λ_h	inflow ratio in hover
ρ	air density
Ω	helicopter rotor angular velocity
ω	vorticity vector

1 Introduction

The NLR has been involved in helicopter-ship qualification testing for over 40 years^[2]. In recent years,

research efforts have been directed towards improving the efficiency of the established procedure with pilot-in-the-loop simulations^[1]. This capability enables safe exploration of candidate flight envelopes in an early stage without depending on the availability of personnel and materiel. Also, environmental conditions can be set that may not occur during flight testing. The research reported here is part of this effort and focuses on the development of a free wake model with real-time capabilities. Based on a literature review^[3], it was decided to focus research on the development of a simplified free wake model where all vorticity is located on a continuous, truncated cylinder that can deform freely under its own influence.

The paper will start with a short introduction of Bézier curves and Non-Uniform Rational B-Spline (NURBS) curves^[9]. NURBS primitives are used in the two sections thereafter to model the geometry of vorticity-carrying elements. In the second section, a NURBS-based vortex ring model is presented. The equations of motion of the vortex ring are derived starting from the vorticity-velocity form of the Navier-Stokes equations. Then, the right-hand side of the resulting equation (velocity calculation using the Biot-Savart law) is elaborated on. This is followed by a verification that the numerically calculated induced velocities converge to analytical results, both in the far field and on the vortex ring itself. Finally, results of time simulations are shown. In the third section, the vorticity-carrying geometry is extended to a circular cylinder to represent the geometry of a rotor wake in hover in a simplified manner. Preliminary results of a simple trim procedure are presented. In the last section of the paper, the current status and the road ahead of the research is discussed.

2 Bézier and NURBS Curves

2.1 Implicit and Parametric Functions

The most common methods to represent curves and surfaces mathematically are the *implicit* and the *parametric* methods.

In the implicit method, a function is used that describes the relation between the independent variables (x and y) of points on the curve. As an example, the unit circle in the xy -plane can be defined by

$$f(x, y) = x^2 + y^2 - 1 = 0 \quad (1)$$

The parametric method on the other hand uses separate (parametric) functions for each axis variable. In two dimensions, the generic form is

$$C(u) = (x(u), y(u)) \quad a \leq u \leq b \quad (2)$$

The first quadrant of the unit circle of Eq. 1 can be written in parametric form as

$$C(u) = (\cos(u), \sin(u)) \quad 0 \leq u \leq \frac{\pi}{2} \quad (3)$$

or alternatively, using $t = \tan(\frac{u}{2})$,

$$C(u) = \left(\frac{1-t^2}{1+t^2}, \frac{2t}{1+t^2} \right) \quad 0 \leq t \leq 1 \quad (4)$$

Bézier, B-spline and NURBS curves and surfaces are all defined as polynomials of one or two parameters. In the following paragraphs, Bézier and NURBS curves will be discussed shortly. The extension to surfaces using a twodimensional array of control points is not discussed here.

2.2 Bézier Curves

2.2.1 Nonrational Bézier Curves

An n^{th} -degree Bézier curve is defined by a set of control points $\{\mathbf{P}_i\}$ and basis functions $\{B_{i,n}(u)\}$,

$$C(u) = \sum_{i=0}^n B_{i,n}(u) \mathbf{P}_i \quad 0 \leq u \leq 1 \quad (5)$$

The basis functions are the n^{th} -degree Bernstein polynomials defined as

$$B_{i,n}(u) = \frac{n!}{i!(n-i)!} u^i (1-u)^{n-i} \quad (6)$$

An example cubic curve and its basis functions are displayed in Fig. 1 and Fig. 2, respectively.

2.2.2 Rational Bézier Curves

It is impossible to represent conics (circles, parabolas, hyperbolas and ellipses) and their three-dimensional extensions (spheres, cylinders, ...) using non-rational polynomials^[9], but as was shown with Eq. 4, this can be achieved using a ratio of two polynomials where each of the coordinate functions has the same denominator.

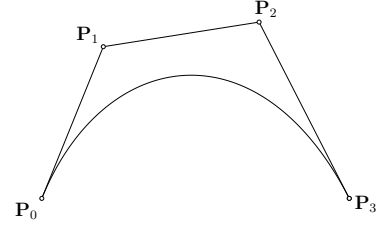


Figure 1: Cubic ($n = 3$) Bézier curve

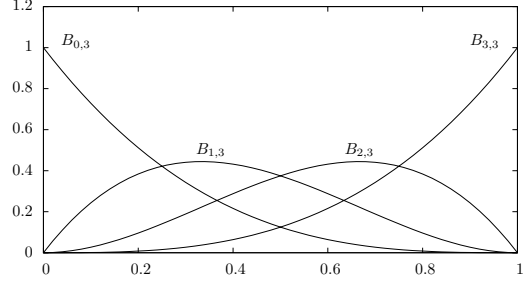


Figure 2: The Bernstein basis functions for $n = 3$.

An n^{th} -degree rational Bézier curve $C(u)$ is defined as

$$C(u) = \frac{\sum_{i=0}^n B_{i,n}(u) w_i \mathbf{P}_i}{\sum_{i=0}^n B_{i,n}(u) w_i} \quad 0 \leq u \leq 1 \quad (7)$$

Again, $\{\mathbf{P}_i\}$ and $\{B_{i,n}(u)\}$ are the control points and basis functions of the curve, and the scalars $\{w_i\}$ are the *weights*. It is assumed that all weights have a value greater than zero, which ensures that the denominator cannot become zero. In terms of rational basis functions $R_{i,n}$,

$$R_{i,n}(u) = \frac{B_{i,n}(u) w_i}{\sum_{j=0}^n B_{j,n}(u) w_j} \quad (8)$$

Eq. 7 can be written in the following compact form

$$C(u) = \sum_{i=0}^n R_{i,n}(u) \mathbf{P}_i \quad 0 \leq u \leq 1 \quad (9)$$

If all weights w_i are equal, the rational curves reduce to the non-rational ones. The addition of non-unity weights to some control points of a curve has the effect of pulling the curve towards those control points.

As an example, the curve in Fig. 1 is modified by assigning a weight of 5 to the third control point \mathbf{P}_2 and the resulting rational cubic Bézier curve is shown in Fig. 3. The rational basis functions of this curve are displayed in Fig. 4.

2.3 B-Spline Basis Functions

In principle, one could use the curves defined in section 2.2 to construct geometry from, but they have

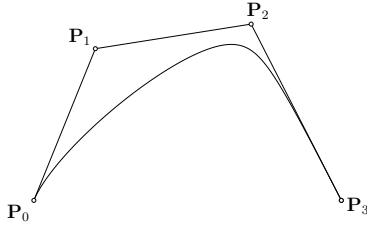


Figure 3: Rational cubic Bézier curve, \mathbf{P}_2 has a weight of 5.

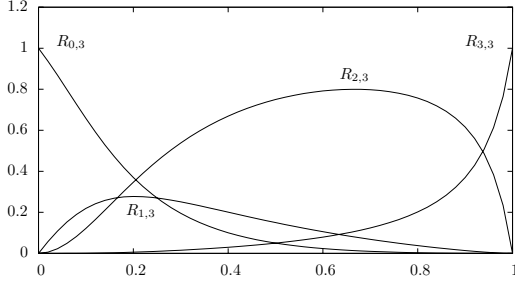


Figure 4: The rational basis functions of the curve displayed in Fig. 3

the disadvantage that modification of a single control point affects the whole curve, i.e. shape control is global. Another drawback is that in order to fit a large number of points with a single curve, a high degree curve is necessary which makes algorithms inefficient. By using piecewise polynomial curves of desired degree and continuity, both drawbacks disappear. The breakpoints in parametric space along the curve where the polynomials are joined are called the *knots*, these are discussed in section 2.3.1. The basis functions themselves are introduced afterwards, in section 2.3.2.

2.3.1 The Knot Vector

The array of non-decreasing parameters that separates the segments is called the *knot vector* U and has the form

$$U = [u_0, u_1, \dots, u_m] \quad \text{with } u_i \leq u_{i+1}, i = 0, \dots, m-1 \quad (10)$$

where u_i are called the *knots* of the knot vector.

A knot vector with equally-spaced knots is said to be *uniform*. In *normalised* form, the first knot u_0 has value 0 and the last knot equals 1, $u_m = 1$. A *clamped* (or *open*) knot vector has a multiplicity of $p+1$ of the first and last values in the knot vector,

$$U = [\underbrace{a, \dots, a}_{p+1}, u_{p+1}, \dots, u_{m-p-1}, \underbrace{b, \dots, b}_{p+1}] \quad (11)$$

where p is the degree of the curve. This ensures that the curve interpolates the end points of the control polygon on which it is defined.

2.3.2 B-Spline Basis Function Definition

The i^{th} B-spline basis function of degree p (order $p+1$), denoted by $N_{i,p}(u)$ is defined recursively by

$$N_{i,0}(u) = \begin{cases} 1 & \text{if } u_i \leq u < u_{i+1} \\ 0 & \text{otherwise} \end{cases}$$

$$N_{i,p}(u) = \frac{u - u_i}{u_{i+p} - u_i} N_{i,p-1}(u) + \frac{u_{i+p+1} - u}{u_{i+p+1} - u_{i+1}} N_{i+1,p-1}(u) \quad (12)$$

As an example, the zeroth, first and second degree basis functions for the knot vector $U = [0, 0, 0, 1, 1, 2, 3, 4, 5, 5, 5]$ are shown below in Figs. 5, 6 and 7, respectively.

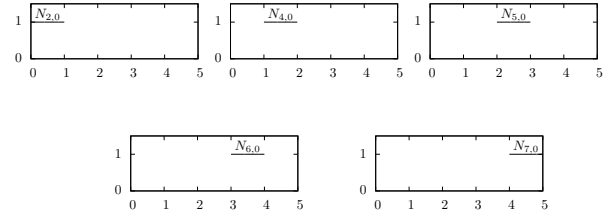


Figure 5: Zero-degree basis functions for the knot vector $U = [0, 0, 0, 1, 1, 2, 3, 4, 5, 5, 5]$

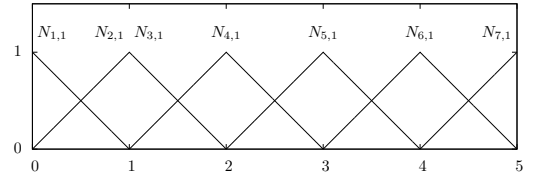


Figure 6: First degree basis functions of the knot vector $U = [0, 0, 0, 1, 1, 2, 3, 4, 5, 5, 5]$

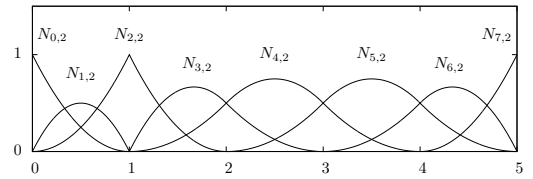


Figure 7: Second degree basis functions of the knot vector $U = [0, 0, 0, 1, 1, 2, 3, 4, 5, 5, 5]$

Some properties of B-spline basis functions are listed below:

- local support: $N_{i,p}$ is non-zero on the interval $[u_i, u_{i+p+1})$;
- partition of unity: for an arbitrary knot span $[u_i, u_{i+1})$, the following equality holds:

$$\sum_{j=i-p}^i N_{j,p}(u) = 1; \quad (13)$$

- non-negativity: $N_{i,p}(u) \geq 0 \quad \forall i, p, u$.

2.4 NURBS Curves

2.4.1 Definition

A p^{th} degree NURBS¹ curve is defined by

$$\mathbf{C}(u) = \frac{\sum_{i=0}^n N_{i,p}(u) w_i \mathbf{P}_i}{\sum_{i=0}^n N_{i,p}(u) w_i} \quad a \leq u \leq b \quad (14)$$

where, as for Bézier curves (Eq. 7), the $\{\mathbf{P}_i\}$ are the control points and the $\{w_i\}$ are the weights. The array $\{N_{i,p}(u)\}$ contains the p^{th} -degree B-spline basis functions defined on the non-periodic and non-uniform knot vector

$$U = [\underbrace{a, \dots, a}_{p+1}, u_{p+1}, \dots, u_{m-p-1}, \underbrace{b, \dots, b}_{p+1}] \quad (15)$$

Just as in the case of rational Bézier curves, Eq. 14 can be written as a non-rational, piecewise polynomial curve using rational basis functions,

$$\mathbf{C}(u) = \sum_{i=0}^n R_{i,p}(u) \mathbf{P}_i \quad (16)$$

where

$$R_{i,p}(u) = \frac{N_{i,p}(u) w_i}{\sum_{j=0}^n N_{j,p}(u) w_j} \quad (17)$$

2.4.2 Construction of NURBS Circles

There are multiple methods that can be used to construct circles using NURBS curves^[8]. One of the most straightforward methods uses a set of rational quadratic Bézier arcs pieced together by a knot vector with double internal knots.

As an example, a circle constructed from four rational Bézier segments is shown in Fig. 8 and the rational basis functions are displayed in Fig. 9.

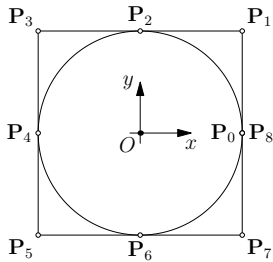


Figure 8: NURBS circle using four rational quadratic Bézier segments.

¹A NURBS curve reduces to a B-spline curve for the case where all the weights $\{w_i\}$ are equal. B-spline curves will not be discussed separately.

The weights for the even-numbered control points equal one, and the weights for the odd-numbered control points can be calculated using

$$w_i = \cos \theta \quad (18)$$

where θ is the angle formed by the triplets $\angle \mathbf{P}_i \mathbf{P}_{i-1} \mathbf{P}_{i+1}$ with \mathbf{P}_i one of the odd-numbered control points. In case of a four-segment (9-point) circle (Fig. 8), the angle is 45° , so that the weights of the odd-numbered control points equal $\frac{\sqrt{2}}{2} \approx 0.7071$. As the number of Bézier segments is increased, the weights of the odd-numbered segments converge to one, since the angle that is spanned per segment (Eq. 18) approaches zero.

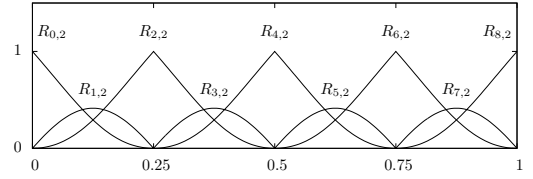


Figure 9: Rational basis functions of the circle shown in Fig. 8.

3 NURBS-based Vortex Ring Model

In this section, a vortex ring model will be derived using the four-segment NURBS ring shown in Fig. 8. First, the equations of motion for a NURBS curve will be derived. After that, some aspects of induced velocity calculation using the Biot-Savart law will be discussed, including core models to correct the unrealistic values of the Biot-Savart law close to the vortex center line. This will be followed by results of a time simulation with multiple NURBS-based vortex rings.

3.1 Equations of Motion

The Navier-Stokes equation for an incompressible flow expressed in velocity-vorticity form governs the evolution of the vorticity field^[14],

$$\frac{\partial \boldsymbol{\omega}}{\partial t} = -(\mathbf{v} \cdot \nabla) \boldsymbol{\omega} + (\boldsymbol{\omega} \cdot \nabla) \mathbf{v} + \nu \Delta \boldsymbol{\omega} \quad (19)$$

The right-hand side terms account for convection, strain (stretching) and vorticity diffusion, respectively. It is assumed that the complete fluid region is inviscid except for regions close to vortex filaments from which follows that they move as a material line at the local velocity (Helmholtz's second law). For a vortex ring in unbounded space, this means that it will propel itself along its centreline. The solution to this problem is described by the convection equation,

$$\frac{d\mathbf{r}}{dt} = \mathbf{v} \quad \mathbf{r}(t=0) = \mathbf{r}_0 \quad (20)$$

where \mathbf{v} is the local velocity at a point on a filament and \mathbf{r}_0 is the initial position of the filament.

The position of a fixed point on a NURBS curve can be calculated using Eq. 16, which is repeated here in a slightly modified (time-dependent) version,

$$\mathbf{C}(u, t) = \sum_{i=0}^n R_{i,p}(u) \mathbf{P}_i(t) \quad (21)$$

Taking the derivative of this equation with respect to time gives

$$\frac{d\mathbf{C}}{dt}(u, t) = \sum_{i=0}^n R_{i,p}(u) \frac{d\mathbf{P}_i}{dt}(t) \quad (22)$$

or

$$\dot{\mathbf{C}}(u, t) = \sum_{i=0}^n R_{i,p}(u) \dot{\mathbf{P}}_i(t) = \mathbf{R}(u) \dot{\mathbf{P}}(t) \quad (23)$$

where the rational basis functions are written in matrix form. Combining Eq. 23 with Eq. 20 results in the following system of equations

$$\mathbf{R}(u) \dot{\mathbf{P}}(t) = \mathbf{V}(u, t) \quad (24)$$

For a set of $n + 1$ control points, the induced velocity must be calculated at an equal amount of points on the vortex ring itself. For the nine-point NURBS circle shown in Fig. 8, the following array of nine parametric points is used,

$$U = \left[0, \frac{1}{8}, \frac{1}{4}, \frac{3}{8}, \frac{1}{2}, \frac{5}{8}, \frac{3}{4}, \frac{7}{8}, 1 \right] \quad (25)$$

which gives nine points uniformly distributed on the circle. Assuming that the induced velocity due to the whole vortex ring at the parametric points is known (see section 3.2), the equivalent induced velocity at the control points can be found to be

$$\dot{\mathbf{P}}(t) = \mathbf{R}^{-1}(u) \mathbf{V}(u, t) \quad (26)$$

As every control point has three coordinates, the above matrix multiplication must be performed three times, once for each coordinate x , y and z .

3.2 Induced Velocity Calculation

3.2.1 Biot-Savart Law for a Parametric Curve

The velocity increment $\Delta \mathbf{v}$ induced at a point P by an infinitesimal segment of a curved vortex filament can be calculated using the Biot-Savart law^[5],

$$\Delta \mathbf{v} = \frac{\Gamma}{4\pi} \frac{d\mathbf{l} \times (\mathbf{r}_P - \mathbf{r}_l)}{|\mathbf{r}_P - \mathbf{r}_l|^3} = \frac{\Gamma}{4\pi} \frac{d\mathbf{l} \times \mathbf{r}}{|\mathbf{r}|^3} \quad (27)$$

where $\mathbf{r} = \mathbf{r}_P - \mathbf{r}_l$, the position of the target point P relative to the point on the vortex line and $d\mathbf{l}$ is the tangent direction on the vortex filament. The induced velocity of the complete curved vortex line

at a target point P is the integral of Eq. 27 over the vortex filament C ,

$$\mathbf{v} = \frac{\Gamma}{4\pi} \int_C \frac{d\mathbf{l} \times \mathbf{r}}{|\mathbf{r}|^3} \quad (28)$$

For a parametric curve $C(u)$, Eq. 27 can be written as

$$\Delta \mathbf{v}(u) = \frac{\Gamma}{4\pi} \frac{d\mathbf{l}(u) \times \mathbf{r}(u)}{|\mathbf{r}(u)|^3} \quad (29)$$

where $d\mathbf{l}(u) = dC(u)/du$, the derivative of the curve at the parametric point u . Then, for m quadrature points \mathbf{u}_i on the vortex line the induced velocity increment $\Delta \mathbf{v}_i$ is calculated and using an m -point quadrature rule, the Biot-Savart integral is converted into a finite sum,

$$\mathbf{v} = \sum_{i=1}^m w_i \Delta \mathbf{v}_i \quad (30)$$

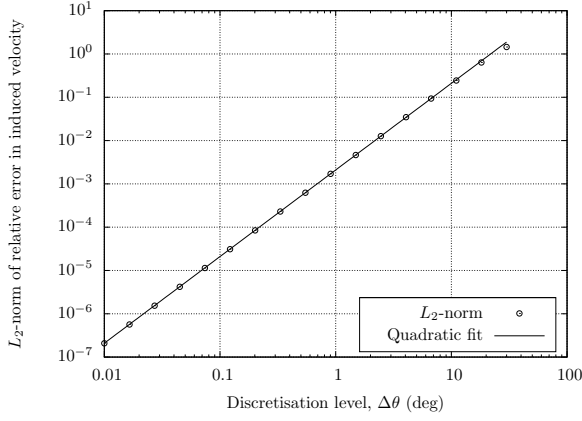
with w_i the weights of the quadrature rule.

The accuracy of the induced velocity calculations using the method described here is quantified below.

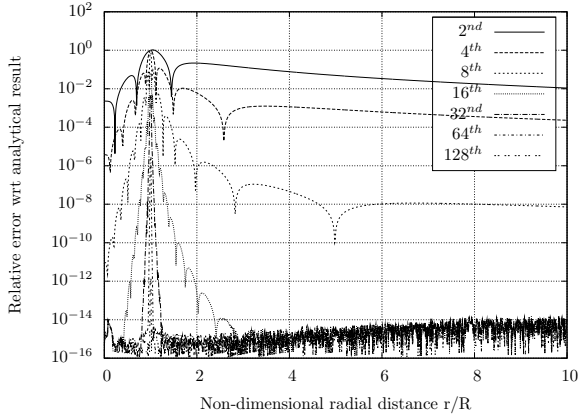
Starting at the centre of the vortex ring, the induced velocity at a set of points on a radial of the ring is calculated using the method described in the previous paragraphs and the classical *straight-segment* approach as described in literature^[5,6]. Results in terms of the L_2 -norm of the relative error of induced velocity for the segmentation method are shown in Fig. 10a for various discretisation levels (between 12 and 36000 segments). For the NURBS-based method, the relative error is shown in Fig. 10b for different quadrature orders. From these figures, it is clear that the segmentation method (Fig. 10a) shows a second-order trend: a ten-fold increase in the number of segments reduces the relative error by a factor of 100. Still, millions of segments would be needed to get results accurate to machine precision. The quadrature method (Fig. 10b) is clearly superior for points that are not too close to the vortex ring. Results calculated using a 32nd-order rule (for a total of 128 Biot-Savart law evaluations) are accurate to machine precision everywhere in the field except for a region close to the vortex ring itself. The slow convergence near the vortex ring is due to the use of fixed-order rules. The efficiency of the NURBS-based quadrature method can be greatly increased by employing adaptive quadrature rules where the required accuracy is set instead of the method order.

3.2.2 Core Model

For a target point that approaches the vortex ring, the induced velocity calculated with Eq. 29 increases unbounded. On the vortex ring itself, the induced velocity is infinite. In literature, this unrealistic behaviour is corrected by regularising the Biot-Savart law with a model that represents the viscous effects inside the vortex core. One of the first researchers to



(a) L_2 -norm of relative error of induced velocity for segmented vortex ring method as a function of the discretisation.



(b) Relative error of induced velocity for the NURBS-based vortex ring method for various quadrature orders.

Figure 10: Convergence induced velocity calculations of segmentation method (a) and quadrature-based method (b) to the potential values in the plane of a vortex ring.

use such a model was Scully^[13] who introduced the following swirl velocity profile

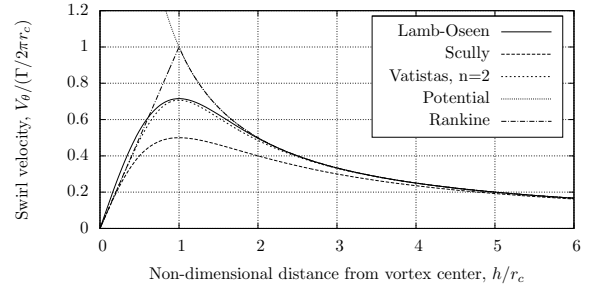
$$V_\theta(\bar{r}) = \frac{\Gamma}{2\pi r_c} \frac{\bar{r}}{1 + \bar{r}^2} \quad (31)$$

Other profiles have been defined by Rankine^[12], Lamb and Oseen^[12] and Vatisas^[15]. For these models, the velocity profile is shown in Fig. 11a as a function of non-dimensional distance from the core centre. The convergence to the potential reference of the Scully, Vatisas ($n = 2$) and the Lamb-Oseen model are displayed in Fig. 11b. For the Vatisas core model (that reduces to other models for specific values of its parameter n), Eq. 29 is modified as follows

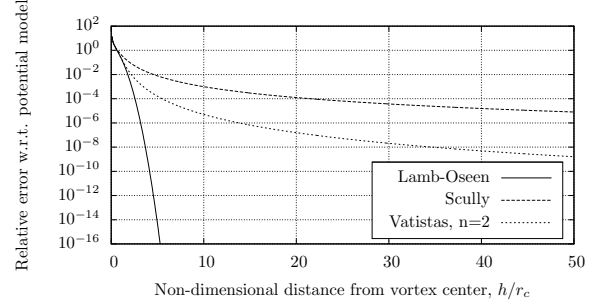
$$\Delta \mathbf{v} = \frac{\Gamma}{4\pi} \frac{|\mathbf{r}(u)|^2}{(r_c^{2n} + |\mathbf{r}(u)|^{2n})^{1/n}} \frac{d\mathbf{l}(u) \times \mathbf{r}(u)}{|\mathbf{r}(u)|^3} \quad (32)$$

where $|\mathbf{r}|$ is the radial distance. This is different from the correction as found in literature^[6]

$$\Delta \mathbf{v} = \frac{\Gamma}{4\pi} \frac{h^2}{(r_c^{2n} + h^{2n})^{1/n}} \frac{d\mathbf{l}(u) \times \mathbf{r}(u)}{|\mathbf{r}(u)|^3} \quad (33)$$



(a) Non-dimensional swirl velocity profile for various vortex core models.



(b) Convergence of the core models to the potential model.

Figure 11: Non-dimensional swirl velocity profiles of various vortex core models (a) and their convergence to the potential model (b).

where the perpendicular distance h is used unconditionally. The difference is illustrated in Fig. 12, the gray area is the region where the core correction model modifies the potential induced velocity value. If the perpendicular distance is used unconditionally (Fig. 12a), this area extends to infinity. The con-

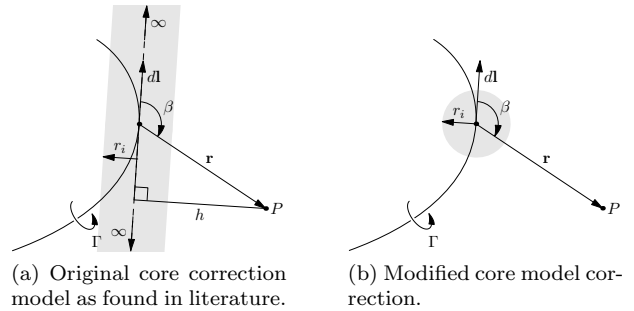
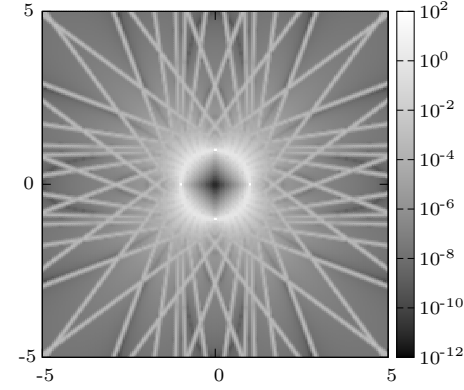


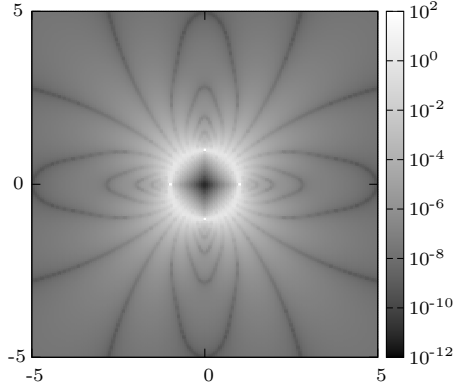
Figure 12: A curved vortex filament with the regularisation region of the core model corrections shown in gray.

sequence of this model is shown in Fig 13a, that shows the logarithm of the relative error in induced velocity in the plane of the vortex ring with a Lamb-Oseen core ($r_c = 0.025R$) for an eighth-order Gauss quadrature rule (32 Biot-Savart law evaluations per target point). The result with the core correction model as given in Eq. 32 is shown in Fig. 13b. For the original core correction model, an error remains along the tangent lines of the quadrature points. When increasing the quadrature order to get more accurate results, one would notice that for a larger percentage

of points outside the vortex ring, the error would not decrease.



(a) Original core correction model, using the perpendicular distance h .



(b) Modified core correction model, using the radial distance $|r|$.

Figure 13: Relative error in induced velocity in the plane of the vortex ring for a vortex ring with a Lamb-Oseen core ($r_c = 0.025R$) for a quadrature order of 8 (32 Biot-Savart evaluations per target point).

When calculating the self-induced velocity of a viscous vortex ring using the core correction models of Eqs. 32 and 33, different results are found.

The theoretical self-induced velocity of a viscous vortex ring with a Rankine core^[12] is given as

$$V_z = \frac{\Gamma}{4\pi R} \left(\log \frac{8R}{r_c} - \frac{1}{4} \right) + O(r_c/R) \quad (34)$$

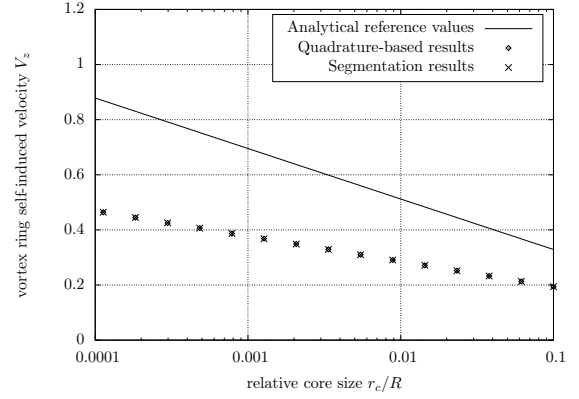
With a relative core size of 0.01 ($r_c/R = 0.01$), unit vorticity strength and unit ring radius, this gives

$$V_z = 0.51205 \approx 0.51 \quad (35)$$

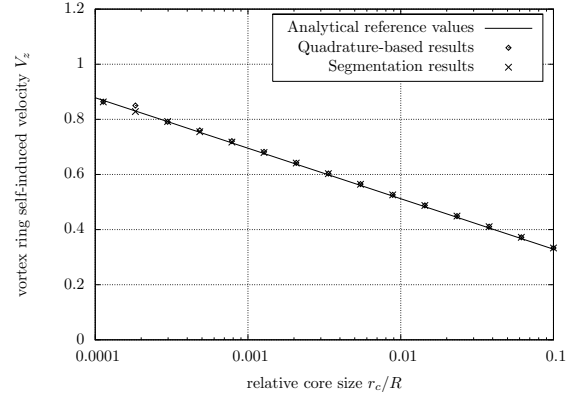
Using the original core correction model (Eq. 33), the induced velocity is found to be $V_z \approx 0.284$ whereas using Eq. 32 gives a value of $V_z \approx 0.516$. The trend as a function of relative core size is shown for both models in Fig. 14, that shows results for both the NURBS-based approach and the classical method using straight line segments.

3.2.3 Time Simulations

Time simulations are performed for a period of 10 seconds using a step size of 0.1 seconds. The integrator used is a standard fourth-order Runge-Kutta



(a) Self-induced velocity prediction with original core correction model.



(b) Self-induced velocity prediction with modified core correction model.

Figure 14: Self-induced velocity of a viscous vortex ring as a function of relative core size for the original (a) and modified (b) core correction model.

method. Knowing that the theoretical self-induced velocity of a vortex ring with a Rankine core model ($r_c/R = 0.05$) is approximately 0.384^[12], a single ring should move a total distance of approximately 3.84 meter if viscous effects are neglected. The position of the vortex ring as a function of time is shown in Fig. 15 together with the reference values. At time $t = 10s$, the z-coordinate of the centre of the ring is located at $z = 3.881003$ which only differs 4 cm with the reference value of 3.84 meter. This is well within the bounds of the accuracy of the reference value.

When two identical vortex rings are placed adjacent to one another in an inviscid fluid, they will leapfrog indefinitely^[11]. For vortices in an incompressible fluid, a change in length (circumference) of a vortex ring should be accompanied by a change in core size to allow the circulation to remain constant. Using a pair of the vortex rings similar to the one used in the previous simulation, a new simulation is performed. The second, identical ring is placed $0.5R$ in front of the first ring (in Fig. 16, a side view is shown). In this situation, the back ring will start moving to the right and inward, while the second ring moves to the right and outward. The speed of the front ring will be reduced considerably which makes it possible for the ring in the back to overtake it. At this point, the outer

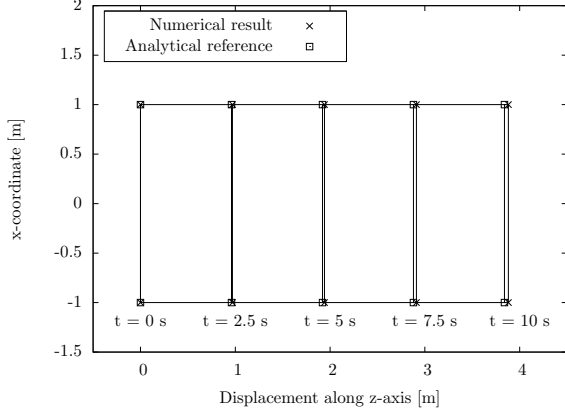


Figure 15: Comparison of the position of a single vortex ring in time calculated analytically and numerically.

ring changes direction rather abruptly and starts moving inward again. The inner ring (which has a higher velocity) starts moving outward and both rings end up switching places (front ring becomes back ring and vice versa). In a stable numerical scheme, this leapfrogging motion continues indefinitely.

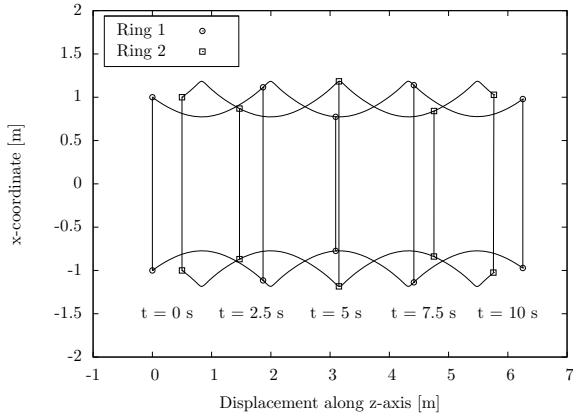


Figure 16: Sideview of leapfrogging vortex rings during a 10 second time simulation.

4 Rotor Wake in Hover

In this section, the vorticity-carrying geometry is extended to a surface. The wake generated by a helicopter rotor in hover is represented in a simplified manner as a continuous cylindrical surface that only carries the trailing vorticity of the tip vortices. First, the amount of vorticity that is released into the wake is determined analytically.

4.1 Vorticity Density in the Wake

Derive how much vorticity is released in the wake per second and what this gives for its density on the wake surface (also list all assumptions).

It is assumed that the thrust required for a helicopter to hover out of ground effect is equal to the weight of the helicopter. Then, the induced velocity v_h can be found to be

$$v_h = \sqrt{\frac{T}{2\rho\pi R^2}} \quad (36)$$

In dimensionless form, Eq. 36 becomes

$$\lambda_h = \sqrt{\frac{C_T}{2}} \quad (37)$$

where the thrust coefficient C_T is defined as

$$C_T = \frac{T}{2\pi R^2(\Omega R)^2} \quad (38)$$

It is assumed that the bound circulation along the span of a rotor blade is constant (i.e., a linear variation in lift). Then, an N -bladed rotor releases N vortices with strength Γ at the blade tips. In a single revolution, these tip vortices can be replaced by N vortex rings of strength Γ or a single vortex ring of strength $N\Gamma$. Then, in a single second, a vortex ring with strength $\frac{N\Gamma}{2\pi}\Omega$ is released in the wake. In hover, the transport speed of this vortex is given by Eq. 36 from which follows that the vorticity density on the wake is

$$\gamma = \frac{N\Gamma\Omega}{2\pi v_h} \quad (39)$$

The tip vortex strength is related to the thrust by

$$T = \frac{1}{2}\rho N\Gamma\Omega R^2 \quad (40)$$

Combining Eq. 40 with Eq. 39 gives

$$\gamma = \frac{C_T(\Omega R)^2}{v_h} \quad (41)$$

4.2 Actuator Disk Vortex Wake Model

A description of the complete actuator disc vortex theory of the rotor in hover is given in Johnson^[4]. Here, a simplified model will be used without the axial root vortex and axial sheet vorticity. For a four-bladed helicopter rotor similar to the Puma helicopter^[7], a simplified wake model is constructed as shown in Fig. 17a. The wake consists of the same circle as shown before in Fig. 8 extruded in the Z -direction. The control points in the z -direction are distributed according to

$$\mathbf{z} = \frac{(1 - \cos(\pi\mathbf{x}))}{2} \quad (42)$$

where \mathbf{x} is an array of uniformly distributed numbers in the range $[0 : 1]$. In total, the cylindrical surface is defined with $9 \times 13 = 117$ control points.

The horizontal plane halfway the wake tube denotes the division of the wake in a near and far wake part.

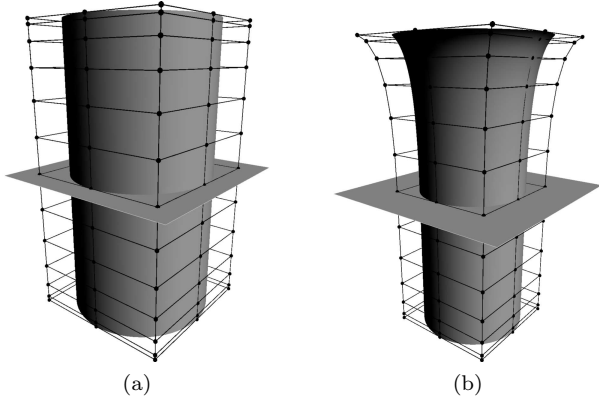


Figure 17: Initial (a) wake of a rotor in hover, wake length $= 2R$ and final (b) wake after a single iteration.

Due to the lack of a robust, adaptive quadrature method in 2D at the time of writing, the current trim procedure is somewhat different than what will be used in the future. It uses Helmholtz’s law that states that the wake geometry should be a streamline and it is explained in the following paragraph.

For every control point that is used to construct the wake geometry, a parametric point on the wake surface is determined. The square rational basis function matrix $\mathbf{R}(u, v)$ is constructed for these points and its inverse is calculated. Due to size constraints, the actual matrices (117×117) are not shown here. Instead, Fig. 18 shows the sparsity patterns of $\mathbf{R}(u, v)$ and its inverse, where the black parts denote nonzero matrix elements.

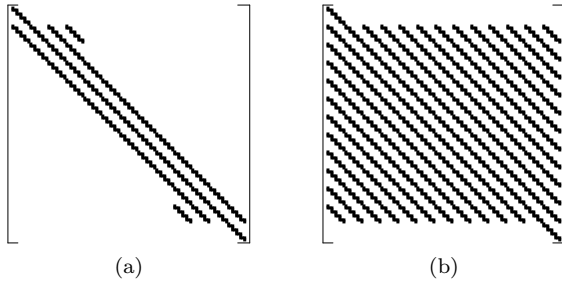


Figure 18: Sparsity patterns of the rational basis function matrix (a) and its inverse (b) for the cylindrical surface shown in Fig. 17, size: (117×117).

Starting near the tip path plane (upper side of the cylinders in Fig. 17), streamlines are traced through the wake downward until they pass the plane halfway the wake. The lateral positions of the parametric points on the wake surface are interpolated on these streamlines and the control point positions are updated using the inverse of the rational basis function matrix. This is shown in Fig. 17b. The induced velocity calculations used to trace the streamline use a 2D (parametric surface) equivalent of the Biot-Savart law on a parametric curve (Eq. 29) with the vorticity strength Γ replaced by the vorticity density γ (Eq. 41). A two-dimensional cross section of the wake and its flow field is shown in Fig. 19. According

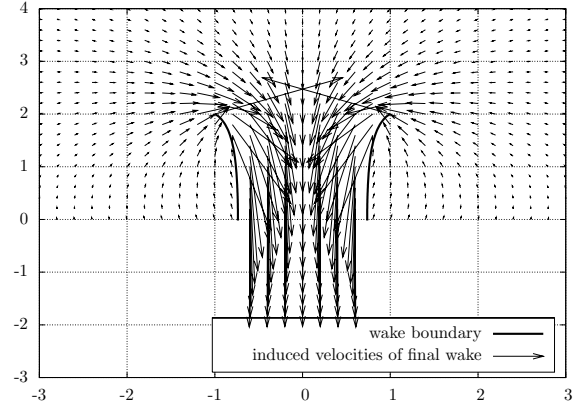


Figure 19: Induced velocity near the rotor wake displayed in Fig. 17b

to actuator disk theory, the induced velocity in the fully developed wake downstream of the rotor is twice the induced velocity at the rotor itself^[4]. Since the flow is assumed to be incompressible, the wake cross sectional area should decrease. As a result, the wake radius downstream of the rotor is found to be

$$R_\infty = \sqrt{\frac{R^2}{2}} = \sqrt{\frac{1}{2}}R \approx 0.707R \quad (43)$$

The actual wake radius as shown in Figs. 17b and 19 is somewhat larger at $0.73R$. It is expected that an iterative trim procedure where the vorticity density on the wake is kept compatible with the wake velocity may give results closer to the theoretical value. The induced velocity in the far field below the rotor (here at two rotor radii below the tip path plane) should be twice the value at the tip path plane. From inspection of Fig. 19, one can conclude that this is indeed the case.

5 Discussion

For one-dimensional cases, such as presented in section 3, NURBS-based vortex simulations prove to be more efficient and accurate than the classical segmentation approach. The reason for this is twofold; the use of NURBS primitives allows one to model the (initial) vorticity-carrying wake structure exactly and the use of numerical quadrature makes it possible to get the most accurate induced velocity values for a fixed number of Biot-Savart function evaluations. Furthermore, the $O(N^2)$ nature of the problem is reduced to an $O(NM)$ problem (where $M \ll N$) since for an accurate representation of the geometry, only a limited number of Lagrangian markers are needed.

Future research will focus on the following topics:

Adaptive quadrature methods If the required accuracy of the induced velocity calculations is a user-settable parameter instead of the order of the

quadrature rule, one can easily trade accuracy for speed in a controlled way.

Rotor trim Before the start of a simulation, the rotor wake should be trimmed to a steady condition. Care must be taken to keep the vorticity density on the vortex sheet consistent with the amount of vorticity that is released from the rotor into the wake.

Interface with Flight Dynamics Models Information must be passed between the flight dynamics model (FDM) and the wake model. From the FDM to the wake, newly created vorticity is passed. The other way around, the influence of the wake at the rotor blades (and other components) must be known. Instead of directly calculating the induced velocity at a rotor blade segment position, induced velocity values will be calculated at a set of points in the rotor tip path plane. These values are then used to identify the coefficients of an inflow distribution (such as the one from Pitt and Peters^[10]). These coefficients are then used to determine the actual values of the induced velocity at the individual blade segments.

Validation and Demonstration of Real-Time Capabilities Once it is verified that results of the wake (both static and dynamic) are consistent with results as found in literature, real-time capabilities should be demonstrated. I.e., a single update of the wake should take less time than the integration time step of the parent simulation.

References

- [1] P. J. A. Booij, J. F. Hakkaart, A. J. Striegel, and J. van der Vorst. Shaping the Dutch Helicopter-Ship Qualification Approach to Future Needs. In *Proceedings of Aero India*, Bangalore, India, February 2007. National Aerospace Laboratory NLR - The Netherlands, Ministry of Defense, India.
- [2] R. Fang and P. J. A. Booij. Helicopter-Ship Qualification Testing – The Dutch Clearance Process. In *Proceedings of the 62nd Annual Forum of the American Helicopter Society*, Phoenix, AZ, May 2006.
- [3] W. R. M. Van Hoydonck, H. Haverdings, and M. D. Pavel. A Review of Rotorcraft Wake Modeling Methods for Flight Dynamics Applications. In *Proceedings of the 35th European Rotorcraft Forum*, Hamburg, Germany, September 2009.
- [4] W. Johnson. *Helicopter Theory*. Princeton University Press, Princeton, New Jersey, 1980.
- [5] J. Katz and A. Plotkin. *Low Speed Aerodynamics*. Cambridge University Press, Cambridge, UK, 2nd edition, 2001.
- [6] J. G. Leishman. *Principles of Helicopter Aerodynamics*. Cambridge Aerospace Series. Cambridge University Press, Cambridge, 2nd edition, 2006.
- [7] G. D. Padfield. *Helicopter Flight Dynamics*. Blackwell Science Ltd., Oxford, 2000.
- [8] L. Piegl and W. Tiller. A Menagerie of Rational B-Spline Circles. *IEEE Computer Graphics and Applications*, 9(5):48–56, September 1989.
- [9] L. Piegl and W. Tiller. *The NURBS Book*. Springer-Verlag, Berlin, 2nd edition, 1997.
- [10] D. M. Pitt and D. A. Peters. Theoretical Prediction of Dynamic – Inflow Derivatives. *Vertica*, 5:21–34, 1981.
- [11] N. Riley and D. P. Stevens. A Note on Leapfrogging Vortex Rings. *Fluid Dynamics Research*, 11(5):235–244, May 1993.
- [12] P. G. Saffman. *Vortex Dynamics*. Cambridge University Press, 1992.
- [13] M. P. Scully. Computation of Helicopter Rotor Wake Geometry and Its Influence on Rotor Harmonic Airloads. Technical Report ASRL TR 178-1, Massachusetts Institute of Technology, Massachusetts, CA, March 1975.
- [14] L. Ting, R. Klein, and O. M. Knio. *Vortex Dominated Flows: Analysis and Computation for Multiple Scale Phenomena*, volume 161 of *Applied Mathematical Sciences*. 2007.
- [15] G. H. Vatistas, V. Kozel, and W. C. Mih. A Simpler Model for Concentrated Vortices. *Experiments in Fluids*, 11(1), April 1991.